Environ Fluid Mech (2016) 16:1087–1110
DOI 10.1007/s10652-016-9466-z

ORIGINAL ARTICLE

Self-similarity and scale effects in physical modelling of hydraulic jump roller dynamics, air entrainment and turbulent scales

Hang Wang[1] · **Hubert Chanson**[1]

Received: 11 October 2015 / Accepted: 16 June 2016 / Published online: 29 June 2016
© Springer Science+Business Media Dordrecht 2016

Abstract A physical study of hydraulic jump is often undertaken using down-scaled Froude-similar models with Reynolds numbers much smaller than in prototype (e.g. spillway stilling basins). The potential viscous scale effects may affect a number of physical processes including turbulence development and air entrainment, thus challenging the extrapolation of laboratory data to the prediction of prototype conditions or justification of numerical modelling. This paper presents an experimental study of hydraulic jumps with a particular focus on the scale effects in terms of free-surface fluctuation and deformation, bubble advection and diffusion, bubble-turbulence interaction and turbulence dissipation. A broad range of free-surface, air–water flow and turbulence properties were measured systematically for Froude numbers from 3.8 to 10 and Reynolds numbers from 2.1×10^4 to 1.6×10^5. Based upon self-similarities in the longitudinal evolution of a number of characteristic flow properties, the analytical expressions of time-averaged roller surface profile, void fraction distribution and longitudinal velocity distribution were derived for given Froude number. The roller surface dynamics were found free of scale effects in terms of fluctuation amplitudes but the characteristic frequencies were scale-sensitive. While some air–water flow parameters such as bubble count rate, bubble chord time distribution and bubble grouping behaviour could only be correctly quantified at full-scale prototype conditions, the aeration level and turbulent scales might be estimated with satisfactory accuracy for engineering applications given a model Reynolds number no less than 4×10 to 6×10^4.

Keywords Hydraulic jumps · Free-surface dynamics · Air entrainment · Turbulent scale · Self-similarity · Scale effects · Physical modelling

✉ Hang Wang
hang.wang@uqconnect.edu.au

[1] School of Civil Engineering, The University of Queensland, Brisbane, QLD 4072, Australia

1 Introduction

A hydraulic jump occurs when an open channel flow changes from supercritical to subcritical [15]. It is a rapidly-varied flow involving air entrainment, turbulent mixing and energy dissipation [33]. Defining the inflow Froude number $Fr_1 = V_1/(g \times d_1)^{0.5}$, where V_1 is the inflow velocity, g is the gravity and d_1 is the inflow depth, a jump with $Fr_1 > 4$ to 4.5 is often employed in man-made hydraulic structures to dissipate the kinetic energy of discharging water [14, 23]. Such type of hydraulic jump is characterised by a marked roller at the transition between the impinging and receiving water bodies, and a depth discontinuity (i.e. jump toe) followed by a turbulent shear layer [16, 22]. A jump may also take place in a partially-filled pipe flow, resulting in noise, vibrations and unnecessary aerification. Despite the theoretical and experimental knowledge gained in the past two centuries, our understanding in detailed flow regimes of mid-to-high-Froude-number hydraulic jumps remains relatively limited, because too many parameters are required to describe all physical processes in such a turbulent multiphase flow.

Physical modelling has been the most reliable approach to investigate hydraulic jumps since the experimental work of Bidone [3]. The first detailed air–water flow measurement was performed by Rajaratnam [29] using conductivity phase-detection probe and Prandtl-Pitot tube to depict the void fraction and velocity distributions. Following Resch and Leutheusser [31] who specified the significance of inflow conditions affecting the air entrainment process, a number of successful characterisations of air–water flow properties and turbulence statistics coupling with bubble transport were reported up to date [26, 36]. The water-phase turbulence was measured for weak jumps with limited aeration (e.g. [21, 34]). The dynamic features of jump roller attracted attention of both physical and numerical modelling researchers [27, 32]. The free-surface profile and fluctuations were measured or simulated, though the analytical studies could hardly take into account the bubble-turbulence interactions, and both experimental and computational investigations were restricted to undersize models [28]. A fundamental issue is the extrapolation of laboratory data to full-scale applications, where self-similarity is regarded as a powerful tool to establish relationships among flow properties at different spatial and temporal scales [1]. Some literature indicated the existence of self-similarities in void fraction and interfacial velocity distributions [9, 20], while others demonstrated significant scale effects for a range of flow properties linked with turbulence development [10].

This paper presents a comprehensive investigation of similitudes and scale effects in physical modelling of hydraulic jumps and their aeration processes. The investigated parameters were expanded beyond air–water flow properties to further cover the jump roller dynamics and turbulent scales. Analytical expressions of void fraction and velocity profiles were developed based on self-similar distributions of characteristic flow properties within a full roller length. The results highlighted a number of key parameters for scale effect assessment in hydraulic jump and other turbulent air–water flows, including the rates of free-surface fluctuation, bubble detection and bubble cluster formation.

2 Dimensional consideration, instrumentation and flow conditions

2.1 Dimensional analysis

For a simplified case where a hydraulic jump is modelled in a horizontal rectangular channel with negligible fluid compressibility and friction resistance, a dimensional analysis indicates that the turbulent air–water flow properties are functions of the spatial positions, inflow conditions and dominant dimensionless parameters including the Froude and Reynolds numbers [15]. Herein the turbulent air–water flow properties include, but are not limited to, the void fraction C, bubble count rate F, roller surface elevation Y_s and its fluctuation y_s', velocity V(x, y, z) and fluctuation v′(x, y, z), turbulent length and time scales, etc. The spatial position is characterised in a dimensionless form $((x - X_t)/d_1, y/d_1, z/d_1)$, where x, y, z are respectively the longitudinal, vertical, transversal positions, X_t is the longitudinal jump toe position and d_1 the inflow depth. The inflow conditions are partially-developed when $\delta/d_1 < 1$, δ being the boundary layer thickness at jump toe, and fully-developed when $\delta/d_1 = 1$. The Froude number, as defined above, is predominant in the physical modelling of open channel flows [19]. For a geometrically-similar down-scaled model with the same fluids as in prototype, the application of Froude similitude implicitly yields a gross underestimate of the Reynolds number $Re = \rho \times V_1 \times d_1/\mu$, where ρ is the water density, μ the water dynamic viscosity and V_1 the inflow velocity [18]. The associated scale effects are critical for turbulent shear flows including hydraulic jumps. The dimensional consideration may also indicate the significance of the Weber number $We = \rho \times V_1^2 \times d_1/\sigma$, σ being the air–water surface tension. Since the use of same fluids in Froude-similar model and prototype yields $We \propto Re^{4/3}$, the viscous effects are considered of higher significance compared to the surface tension in prototype conditions [37, 10].

2.2 Facility and instrumentation

The experiments were performed in a horizontal rectangular channel. The channel was built with an upstream head tank, followed by a 3.2 m long, 0.5 m wide and 0.4 m deep experimental section between an upstream undershoot gate and a downstream overshoot gate (Fig. 1). The rounded edge ($Ø = 0.3$ m) of the upstream gate induced a horizontal impinging flow without contraction. For a given flow rate and upstream gate opening, the roller position was controlled by adjusting the height of the downstream gate. Figure 1 illustrates the experimental setup and some key parameters.

The flow rate was measured with a Venturi meter in the supply pipeline. The inflow depth d_1 and downstream clear-water depth d_2 were measured using a pointer gauge. A series of acoustic displacement meters were used to record the instantaneous water surface positions. The displacement meters emitted acoustic beams and received those reflected by the detected water surface, recording the beam travel distance. One sensor (Microsonic™ Mic+35/IU/TC) was placed horizontally upstream of the jump, recording the longitudinal motion of the jump front close to the toe, and several sensors (Microsonic™ Mic+25/IU/TC) were aligned over the roller centreline, recording the water elevation fluctuations (Fig. 1). All sensors were scanned at 50 Hz for 540 s. Erroneous sample points caused by the spray and droplet projections were removed manually in data post-processing.

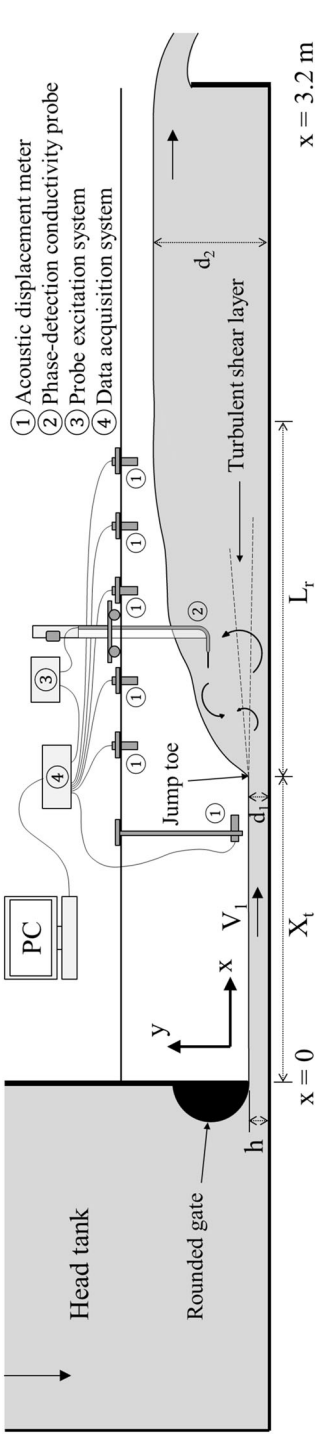

Fig. 1 Definition sketch of experimental setup. X_t longitudinal jump toe position, L_r jump roller length, h upstream gate opening, d_1 inflow depth, V_1 cross-sectional average inflow velocity, d_2 downstream depth

The local air–water flow properties were measured using a dual-tip phase-detection probe. The needle sensor of the probe had a 0.25 mm diameter inner electrode and an external diameter of 0.8 mm. A dual-tip probe was equipped with two such sensors of different lengths. The two sensors were excited simultaneously at a sampling rate of 20 kHz for 45 s.

The phase-detection probe detected the transport of air–water interfaces between the two sensor tips. A correlation analysis between the signals provided statistic information on air–water interfacial velocity and turbulence. The longitudinal interfacial velocity was given by $V = \Delta x/T$, where Δx is the longitudinal probe-tip separation distance and T is the time lag of maximum cross-correlation coefficient. The interfacial turbulence intensity $Tu = v'/V$ was calculated based on the broadening of the correlation functions by assuming a random detection of an infinitely large number of air–water interfaces [12]. An integration of the maximum correlation $(R_{ij})_{max}$ as a function of the probe-tip separation distance Δx yielded the integral turbulent length scale:

$$L_X = \int_0^{\Delta x((R_{ij})_{max}=0)} (R_{ij})_{max} \times d(\Delta x) \quad (1)$$

The integral turbulent length scale is a characteristic length scale of coherent vortical structures in which air–water interfaces are advected. Herein the different values of Δx were achieved using a series of dual-tip probes with Δx from 0 to 29.68 mm. In the present study, both interfacial turbulence intensity and integral turbulent length scale were calculated based on high-pass filtered probe signals (>10 Hz) where the effects of flow instabilities on turbulence characterisation was minimised [36]. The resulted high-frequency turbulence intensity and integral length scale are denoted Tu'' and L_X'' respectively.

Mass conservation was tested against the flow meter measurements based on the void fraction and velocity data given by the phase-detection probe. The agreement was satisfactory, with some scatter related to the incomplete velocity profiles (see below).

Table 1 Flow conditions for Froude-similar free-surface and air–water flow measurements

Reference	Fr_1	Re	h/W	X_t/d_1	Instrumentation
Present study	3.8	3.4×10^4 to 1.6×10^5	0.04 to 0.108	40 ± 2[a]	ADM, 2-PDP
	5.1	4.5×10^4 to 1.4×10^5	0.04 to 0.08	40 ± 2[a]	ADM, 2-PDP
	7.5	3.4×10^4 to 1.4×10^5	0.024 to 0.06	40 ± 2	ADM, 2-PDP
	8.5	7.5×10^4	0.04	41.5	ADM, 2-PDP
	10.0	9.5×10^4	0.04	39.5	ADM, 2-PDP
Chanson and Chachereau [10]	5.1	1.3×10^5	0.072	38	2-PDP
Chanson and Gualtieri [11]	5.1	2.5×10^4 to 6.8×10^4	0.048	20.8 to 41.7	1-PDP
Murzyn and Chanson [24]	5.1	3.8×10^4	0.036	41.7	2-PDP

Fr_1 inflow Froude number, *Re* inflow Reynolds number, *h* upstream gate opening, *W* channel width, *X_t* longitudinal jump toe position, *d_1* inflow depth, *ADM* acoustic displacement meter, *1-PDP* single-tip phase-detection probe (0.35 mm diameter inner electrode), *2-PDP* dual-tip phase-detection probe (0.25 mm diameter inner electrode)

[a] For the highest Reynolds number because of the limitation of channel length: $X_t/d_1 = 22$ ($Fr_1 = 3.8$), 29 ($Fr_1 = 5.1$)

2.3 Flow conditions

An extensive range of experiments were performed, covering Froude numbers from 3.8 to 10 and Reynolds numbers from 2.1×10^4 to 1.6×10^5. All tested flows were characterised by partially-developed inflow conditions. The Froude similitude was tested systematically for three Froude numbers ($Fr_1 = 3.8$, 5.1 and 7.5). Table 1 summarises the experimental flow conditions and includes relevant references.

3 Experimental results and self-similarities

3.1 Free-surface profile

Key dimensions of a hydraulic jump include the conjugate depth ratio d_2/d_1 and the relative roller length L_r/d_1 (Fig. 1), where L_r refers to the longitudinal distance over which the water elevation increases monotonically. For a smooth horizontal rectangular channel, the

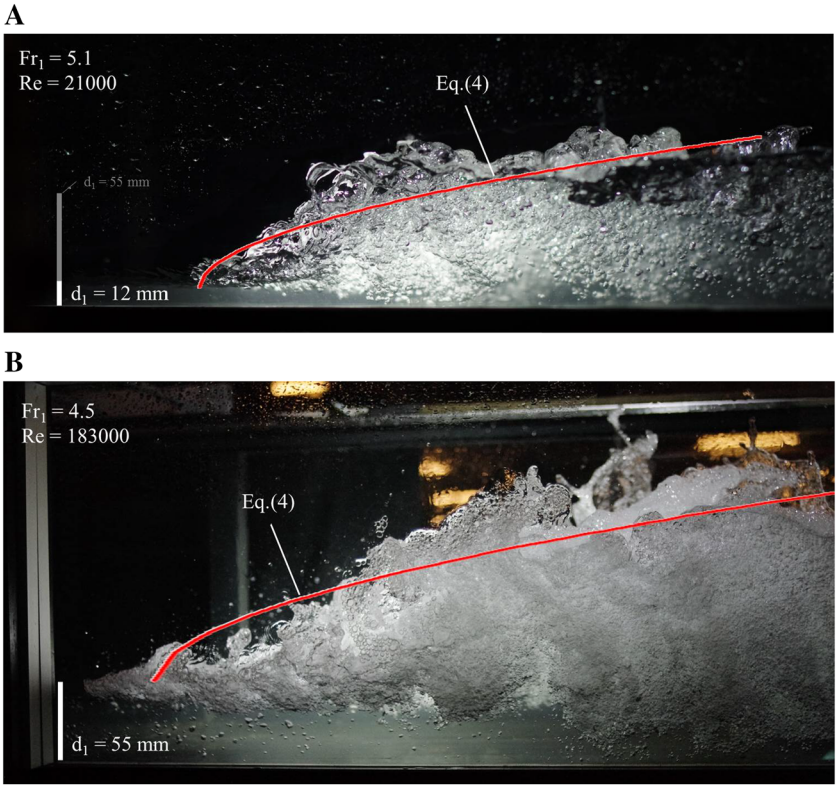

Fig. 2 Side view of hydraulic jumps with close inflow Froude numbers but different Reynolds numbers–comparison with self-similar roller surface profile. Flow from left to right; shutter speed 1/8000 s. **a** $Fr_1 = 5.1$, $Re = 2.1 \times 10^4$, $d_1 = 0.012$ m, $X_t = 0.5$ m. **b** $Fr_1 = 4.5$, $Re = 1.83 \times 10^5$, $d_1 = 0.055$ m, $X_t = 1.25$ m

conjugate depth ratio d_2/d_1 can be simply determined by the mass and momentum conservation equations as a function of the Froude number [2]:

$$\frac{d_2}{d_1} = \frac{1}{2} \times \left(\sqrt{1 + 8 \times Fr_1^2} - 1 \right) \quad (2)$$

The relative jump roller length L_r/d_1 was observed to increase almost linearly with increasing Froude number. A re-analysis of the present experimental data and the data of Murzyn et al. [27], Kucukali and Chanson [17] and Murzyn and Chanson [25] suggested a relationship:

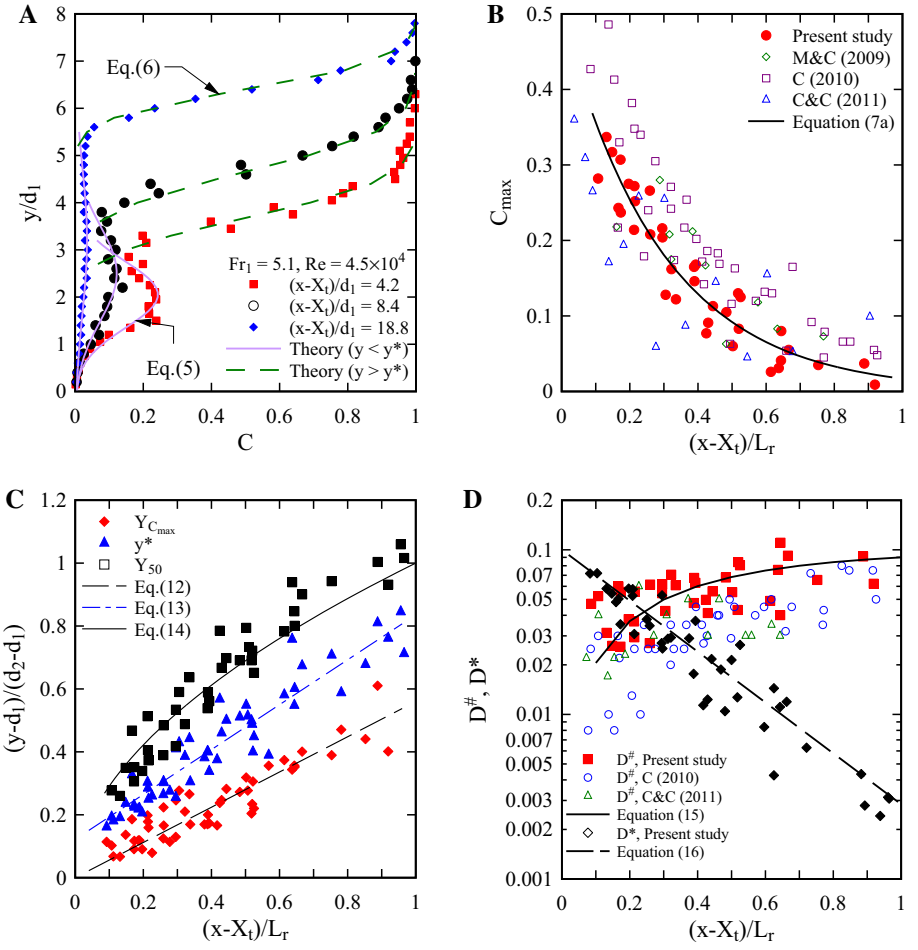

Fig. 3 Time-averaged void fraction distribution and longitudinal variation of characteristic values within the roller length. **a** *Left* vertical distributions of time-averaged void fraction–comparison with analytical solutions. **b** *Right* longitudinal decay in local maximum void fraction along roller length–comparison with data of Murzyn and Chanson [25], Chanson [9], Chachereau and Chanson [8] and exponential fit. **c** *Left* characteristic elevations and best-fit curves. **d** *Right* dimensionless diffusion coefficients–comparison with data of Chanson [9], Chachereau and Chanson [8] and best-fit curves

$$\frac{L_r}{d_1} = 6 \times (Fr_1 - 1) \quad \text{for } 2 < Fr_1 < 10 \tag{3}$$

Equations (2) and (3) implied that the ratio of roller length to downstream depth L_r/d_2 approached an approximate value around $L_r/d_2 \approx 4$ at high Froude numbers, although Eq. (3) was not yet validated for $Fr_1 > 10$.

The time-averaged water elevation above the jump roller exhibited a self-similar roller surface profile for all tested flow conditions. The experimental data followed closely

$$\frac{Y_s - d_1}{d_2 - d_1} = \left(\frac{x - X_t}{L_r}\right)^{0.537} \quad \text{for } 3.8 < Fr_1 < 10,\ 0 < (x - X_t)/L_r < 1 \tag{4}$$

where Y_s stands for the vertical position of water surface from the invert. Considering Eqs. (2) and (3), the dimensionless water elevation Y_s/d_1 at a longitudinal position $(x - X_t)/d_1$ is simply a function of the Froude number Fr_1. Equation (4) is sketched in Fig. 2 for the corresponding Froude numbers, agreed well with the visualisation in spite of the instantaneous roller surface deformation in each photograph.

3.2 Air–water flow properties

3.2.1 Void fraction

In hydraulic jumps, air entrainment takes place at the jump toe and through the roller free-surface (Fig. 2) [35]. The spatial distributions of time-averaged void fraction characterise the bubble advection and diffusion processes in the roller. Figure 3a plots void fraction profiles at three cross-sections in the same flow. For partially-developed inflow conditions, the typical void fraction profile exhibited a bell-shape in the shear flow region, with a local maximum C_{max} at the elevation Y_{Cmax}, and a monotonically increasing distribution across the free-surface region up to unity in air. The boundary between the shear flow and free-surface regions was characterised by a local minimum void fraction at the elevation y*. The shear flow void fraction distribution followed the solution of bubble diffusion equation with the jump toe being the point source of air entrainment [9]:

$$C = C_{max} \times \exp\left(-\frac{1}{4 \times D^{\#}} \times \frac{\left(\frac{y - Y_{Cmax}}{d_1}\right)^2}{\left(\frac{x - X_t}{d_1}\right)}\right) \quad y < y^* \tag{5}$$

where $D^{\#}$ is a depth-averaged diffusivity for $0 < y < y^*$. In the upper free-surface region, an interfacial aeration model suggested a void fraction distribution following the Gaussian error function [6, 26]:

$$C = \frac{1}{2} \times \left(1 + \text{erf}\left(\frac{\frac{y - Y_{50}}{d_1}}{2 \times \sqrt{D^* \times \frac{(x - X_t)}{d_1}}}\right)\right) \quad y > y^* \tag{6a}$$

where Y_{50} is the elevation where $C = 0.5$, D^* is the diffusivity in the free-surface region ($y > y^*$), and the Gaussian error function is defined as

$$\mathrm{erf}(u) = \frac{2}{\sqrt{\pi}} \times \int_0^u \exp(-t^2) \times dt \tag{6b}$$

Equations (5) and (6) are compared with experimental data in Fig. 3a. Figures 3b–d show the longitudinal variations of the key parameters in Eqs. (5) and (6) for $3.8 < Fr_1 < 10$, $3.4 \times 10^4 < Re < 1.6 \times 10^5$. Similar distributions were shown for each parameter over the roller length L_r between different flow conditions, as fitted by Eqs. (7)–(12). In Fig. 3b, the present local maximum void fraction data are compared with the data of Murzyn and Chanson [25] for $5.1 < Fr_1 < 8.3$, Chanson [9] for $5.1 < Fr_1 < 11.2$ and Chachereau and Chanson [8] for $3.1 < Fr_1 < 5.1$. Assuming a pseudo-periodic jump toe oscillation, thus $C_{max}(x = X_t) = 0.5$, the present data was best correlated in terms of the roller length:

$$C_{max} = 0.5 \times \exp\left(-3.4 \times \frac{x - X_t}{L_r}\right) \tag{7a}$$

Equation (7a) may be also written as:

$$C_{max} = 0.5 \times \exp\left(-\frac{1}{1.8 \times (Fr_1 - 1)} \times \frac{x - X_t}{d_1}\right) \tag{7b}$$

In Fig. 3b, the data scatter about Eq. (7a) was mostly related to the scale effects. The uncertainties in roller length estimation may also contribute to the discrepancies between the previous datasets.

Figure 3c shows increasing characteristic elevations Y_{Cmax}, y* and Y_{50} with increasing distance from the toe. The elevations Y_{Cmax} and y* are respectively considered as the centreline and upper boundary of the turbulent shear layer, and they followed some linear increasing trends as the water depth increased and the shear layer expanded:

$$\frac{Y_{C_{max}} - d_1}{d_2 - d_1} = 0.56 \times \frac{x - X_t}{L_r} \tag{8}$$

$$\frac{y* - d_1}{d_2 - d_1} = 0.122 + 0.714 \times \frac{x - X_t}{L_r} \tag{9}$$

The elevation Y_{50} was found close to the time-averaged water depth Y_s measured by acoustic displacement meters. The best-fit curve almost overlapped with the roller surface profile (Eq. 4):

$$\frac{Y_{50} - d_1}{d_2 - d_1} = \left(\frac{x - X_t}{L_r}\right)^{0.536} \tag{10}$$

The diffusivities $D^{\#}$ and D* were deduced for the best-fit void fraction profiles (Fig. 3d). The shear flow diffusivity $D^{\#}$ was typically between 0.02 and 0.1, increasing with increasing distance from the toe, and the free-surface diffusivity D* was between 0.08 and 0.001, decreasing along the roller. A larger Froude number tended to give both relatively higher values of $D^{\#}$ and D*. A coarse data-fit suggested:

$$D^{\#} = 0.1 \times \left(1 - \exp\left(-2.3 \times \frac{x - X_t}{L_r}\right)\right) \quad (11)$$

$$D^{*} = 0.1 \times \exp\left(-3.56 \times \frac{x - X_t}{L_r}\right) \quad (12)$$

A combination of Eqs. (2) to (12) allowed for a prediction of spatial void fraction distributions using the inflow Froude number ($3.8 < Fr_1 < 10$). The analytical model was independent of the Reynolds number. It was tested against the experimental results, yielding an average coefficient of determination $R^2 = 0.90$ for a total of 36 data profiles.

3.2.2 Bubble count rate

The bubble count rate is linked to both local void fraction and turbulent shear stress affecting bubble break-up, coalescence and dispersion. For a given void fraction, the bubble count rate is proportional to the air–water interfacial area. Figure 4a shows typical bubble count rate distributions at different vertical cross-sections in the roller. The data profiles exhibited a bimodal shape, with the lower peak corresponding to the presence of maximum shear stress in the shear layer and the upper peak next to the time-averaged water elevation where $C = 0.3$ to 0.5. The lower peak decreased rapidly in the longitudinal direction as the shear flow turbulence was dissipated and the shear layer was de-aerated by buoyancy.

Figure 4b plots the longitudinal decay of maximum bubble count rate $F_{max} \times d_1/V_1$ over the roller length. The decreasing trend varied significantly among different Froude and Reynolds numbers. Although no physical data was available close to the toe ($0 < (x - X_t)/L_r < 0.1$) because of the toe oscillations, a general variation trend may still be estimated based on an analogy between a hydraulic jump and a vertical plunging jet. A supported planar plunging jet is characterised by similar air entrainment and shear layer

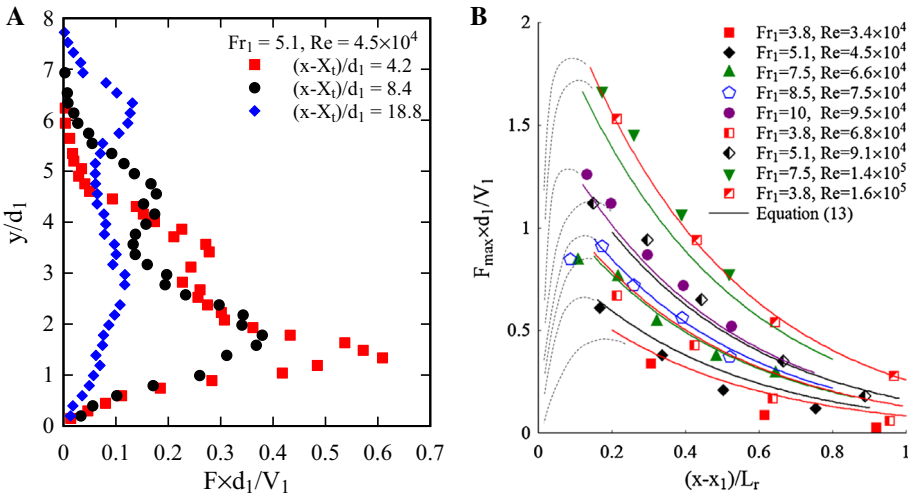

Fig. 4 Bubble count rate distributions and longitudinal decay. **a** *Left* vertical distributions of bubble count rate. **b** *Right* longitudinal decay in maximum bubble count rate along roller length

development processes [4], and the relatively stable flow pattern allows for detailed air–water flow measurements close to the impingement point. Using similar instrumentation, Brattberg and Chanson [5] observed a rapid increase in maximum bubble count rate within a short distance from the impingement point before it decreased with further increasing distance. This reflected a bubble break-up process, which was believed to take place in hydraulic jumps as well. Therefore, the longitudinal variation of maximum bubble count rate was proposed with a unimodal shape, as sketched by dot lines in Fig. 4b. The proposed trends suggested relatively small bubble count rates at the jump toe corresponding to the entrapment of large air pockets, and a sharp increase in bubble quantity as the air pockets were broken into numerous small bubbles by the shear stresses. The largest value of $F_{max} \times d_1/V_1$ was expected to be reached around $0.1 < (x - X_t)/L_r < 0.2$, the magnitude being determined by the Reynolds number. The subsequent decrease followed an exponential decay controlled by the diffusive advection of bubbles, for which the Froude number acted as a predominant factor. The decreasing maximum bubble count rate may be estimated as:

$$\frac{F_{max} \times d_1}{V_1} = \left(0.343 + 0.131 \times \frac{Re}{10^4}\right) \times \exp\left(-\frac{1}{2.67 \times (Fr_1 - 1)} \times \frac{x - x_1}{d_1}\right) \quad \text{for } 0.2 < (x - X_t)/L_r < 1 \tag{13}$$

Equation (13) was derived based upon experimental datasets with $3.8 < Fr_1 < 11.2$ and $3.5 \times 10^4 < Re < 1.6 \times 10^5$. It is plotted in solid lines in Fig. 4b and compared to the present data with the same Froude and Reynolds numbers.

3.2.3 Longitudinal interfacial velocity

The time-averaged longitudinal velocity V was positive in the shear flow region, with a boundary layer developing above the channel bed, and negative in the free-surface recirculation region. An analogy between the impinging flow into the jump roller and a wall jet suggested a velocity distribution following some wall jet equation [9, 30]:

$$\frac{V}{V_{max}} = \left(\frac{y}{Y_{V_{max}}}\right)^{\frac{1}{N}} \quad \text{for } \frac{y}{Y_{V_{max}}} < 1 \tag{14a}$$

$$\frac{V - V_{recirc}}{V_{max} - V_{recirc}} = \exp\left(-\frac{1}{2} \times \left(1.765 \times \left(\frac{y - Y_{V_{max}}}{Y_{0.5}}\right)\right)^2\right) \quad \text{for } \frac{y}{Y_{V_{max}}} > 1 \tag{14b}$$

where V_{max} is the maximum velocity in the lower shear flow, Y_{Vmax} is the corresponding elevation of maximum velocity which also characterises the upper edge of the bottom boundary layer, V_{recirc} is the depth-averaged recirculation velocity, $Y_{0.5}$ is the elevation where $V = (V_{max} - V_{recirc})/2$ and N is a constant between 6 and 10. Equation (14) described a self-similar velocity distribution in a hydraulic jump with a marked roller. The experimental data are plotted in Fig. 5a and compared with Eq. (14b), showing similarities between different Froude and Reynolds numbers as well as different longitudinal positions. The inherent limitation of correlation analysis hindered the derivation of meaningful velocity data in the transition area between positive and negative velocity regions where the instantaneous velocity direction changed frequently and the average velocity was close to zero. The velocity profile in Fig. 5a showed the maximum velocity V_{max} in the lower

shear region and quasi-uniform recirculation velocity V_{recirc} across the free-surface region. Figure 5b plots the longitudinal variation of V_{max} within the roller length, and the corresponding elevation Y_{Vmax} is shown in Fig. 5c together with the elevation $Y_{0.5}$. The depth-averaged ($y > y^*$) recirculation velocity is shown in Fig. 5d for different Froude numbers.

For all flow conditions, the maximum velocity in the shear flow decreased from the supercritical free-stream velocity U at the jump toe to $0.3 \times V_1$ to $0.5 \times V_1$ at the downstream end of roller (Fig. 5b). The longitudinal decay followed a trend:

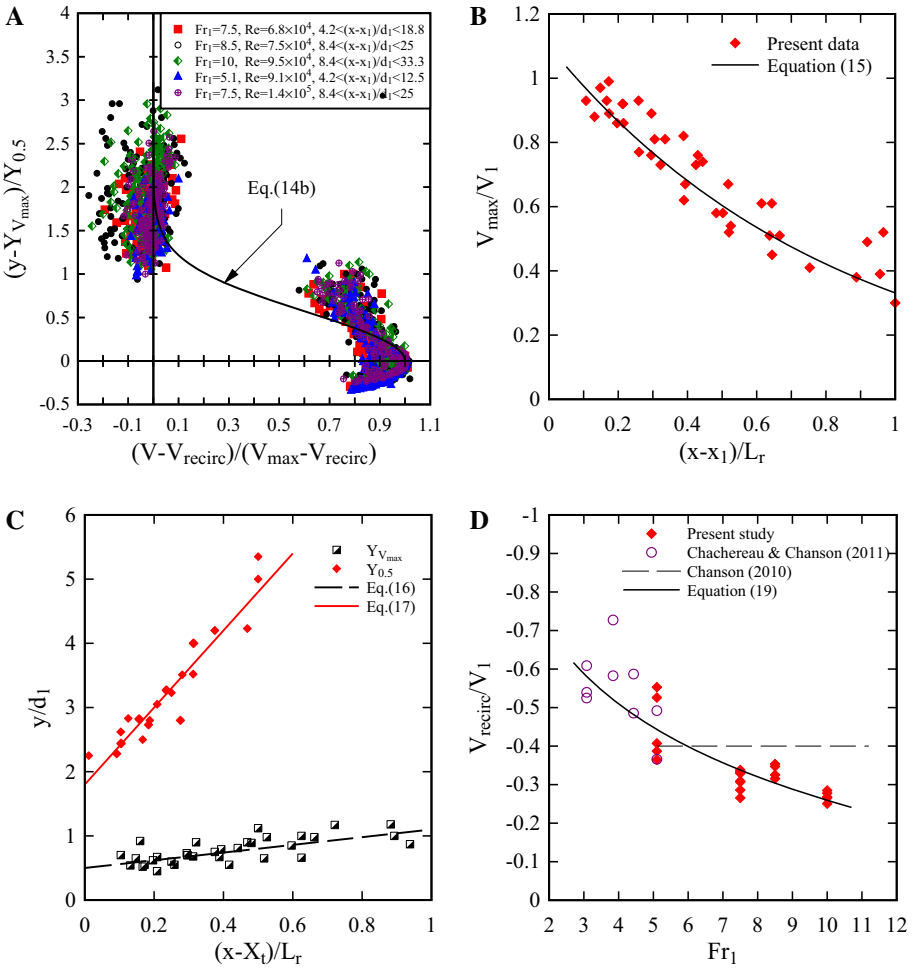

Fig. 5 Time-averaged interfacial velocity profile and characteristic parameters. **a** *Left* self-similar velocity distribution–comparison with the wall jet solution. **b** *Right* longitudinal decay in maximum velocity within the roller length; $3.8 < Fr_1 < 10$, $3.5 \times 10^4 < Re < 1.6 \times 10^5$. **c** *Left* elevations of maximum and zero velocities; $5.1 < Fr_1 < 10$, $6.8 \times 10^4 < Re < 1.4 \times 10^5$. **d** *Right* recirculation velocity–comparison with data of Chachereau and Chanson [8], Chanson [9] and Eq. (19)

$$V_{max} = U \times \exp\left(-1.2 \times \frac{x - X_t}{L_r}\right) \quad \text{for } 3.8 < Fr_1 < 10 \tag{15}$$

where the supercritical free-stream velocity $U \approx 1.1 \times V_1$. The vertical position of maximum velocity Y_{Vmax} increased as the boundary layer developed along the roller (Fig. 5c). The characteristic elevations could be estimated as:

$$\frac{Y_{V_{max}}}{d_1} = 0.5 + 0.6 \times \frac{x - X_t}{L_r} \tag{16}$$

$$\frac{Y_{0.5}}{d_1} = 1.8 + 6 \times \frac{x - X_t}{L_r} \tag{17}$$

Overall the characteristic elevations satisfied a relationship:

$$\frac{Y_{V_{max}}}{d_1} < \frac{Y_{F_{max}}}{d_1} < \frac{Y_{C_{max}}}{d_1} < \frac{y(V = 0)}{d_1} < \frac{y*}{d_1} < \frac{Y_{50}}{d_1} \approx \frac{Y_s}{d_1} \tag{18}$$

where $y(V = 0)$ is the boundary between positive and negative flow regions with zero time-averaged velocity. The reversing velocity was quasi-uniform in each cross-section of the recirculation region, and close depth-averaged values V_{recirc}/V_1 were obtained at different longitudinal positions in the same flow. The data of present study and Chachereau and Chanson [8] suggested a decreasing dimensionless recirculation velocity magnitude with increasing Froude number (Fig. 5d):

$$\frac{V_{recirc}}{V_1} = -0.888 + 0.273 \times \ln(Fr_1) \quad \text{for } 3.1 < Fr_1 < 10 \tag{19}$$

It is noteworthy that flow recirculation only took place within a short distance downstream of the toe for small Froude numbers, and the relative length of reversing flow to entire roller appeared to increase with increasing Froude number, albeit remained less than unity. The recirculation velocity results were quantitatively comparable to the earlier findings $V_{recirc}/V_1 \approx 0.4$ [9]. For comparison, Coakley et al. [13] measured the breaking free-surface velocity with radar instrumentation and found velocity scattering from -1 to 0.5 m/s for approaching velocities from 2.42 to 2.65 m/s. Consequently, the time-averaged longitudinal velocity profile was described by Eqs. (14) to (19), thus can be fully-expressed using the longitudinal position $(x - X_t)/d_1$ and Froude number Fr_1. For all 23 velocity profiles in the present study, the analytical model provided an average coefficient of determination $R^2 = 0.90$. Although three-dimensional turbulent structures were visible in the roller and at the free-surface, the correlation between signals at different transverse positions indicated the time-averaged transverse velocity being zero.

3.2.4 Air entrainment flux

Based upon the void fraction and interfacial velocity measurements, the air entrainment flux was derived from the mass conservation for the air phase. In the presence of distinct flow recirculation, the air flux q_{ent} was calculated in two flow regions:

$$q_{ent}^{(s)} = \int_{y=0}^{y(V=0)} C \times V \times dy > 0 \quad (20a)$$

$$q_{ent}^{(r)} = \int_{y(V=0)}^{Y_{90}} C \times V \times dy < 0 \quad (20b)$$

Herein $q_{ent}^{(s)}$ and $q_{ent}^{(r)}$ denote the entrapped air fluxes in the turbulent shear region ($V > 0$, $q_{ent}^{(s)} > 0$) and recirculation region ($V < 0$, $q_{ent}^{(r)} < 0$) respectively, and Y_{90} is the elevation where $C = 0.9$, considered as the upper boundary of the open homogeneous air–water flow [7]. A definition sketch is shown in Fig. 6a. The experimental data are plotted in Fig. 6b in terms of the longitudinal variations of entrained and recirculation air fluxes. Since the spatial distributions of void fraction and velocity can be predicted based on Eqs. (2) to (19), the air entrainment flux is also predictable for a given Froude number. The air flux prediction varied to some extent between Froude numbers, and a typical longitudinal variation trend is given in Fig. 6b (dashed lines). Overall the experimental data agreed well with the predictions, though the phase-detection probes tended to provide overestimated air fluxes due to the accumulative effects of the scatter in velocity measurement results.

The theoretical prediction suggested a sharp increase in both shear flow and recirculation air fluxes immediately downstream of the toe. The total air flux $|q_{ent}^{(s)}| + |q_{ent}^{(r)}|$ reached a maximum between $(x - X_t)/L_r = 0.2$ and 0.4. Bubbles were driven by buoyancy from the shear layer to the free-surface, and this resulted in a faster longitudinal de-aeration of the shear flow than the upper recirculation region. The air entrainment at the jump toe acted as the source of air flux $q_{ent}^{(s)}$ in the shear layer, and the air flux $q_{ent}^{(s)}$ contributed to part of the recirculating air flux $q_{ent}^{(r)}$ in the free-surface region, the rest part $|q_{ent}^{(r)}| - |q_{ent}^{(s)}|$ being the air–

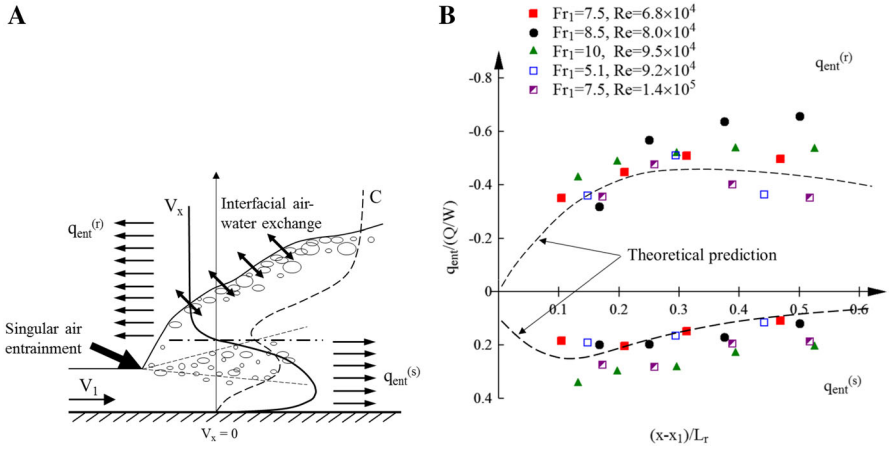

Fig. 6 Longitudinal distribution of air entrainment flux–experimental data and typical theoretical prediction. **a** *Left* sketch of air entrainment and entrapped air flux in hydraulic jump with a marked roller. **b** *Right* longitudinal development of relative air entrainment fluxes to specific water discharge in turbulent shear region and recirculation region

water exchange in the spray region above the bubbly flow. In Fig. 6, $|q_{ent}^{(r)}| - |q_{ent}^{(s)}| > 0$ indicates an extra amount of air entrainment through the roller free-surface.

4 Scale effects and turbulence scales

4.1 Scale effects on roller surface dynamics

The dynamic characteristics of jump roller included the vertical water depth fluctuations and horizontal jump toe oscillations. The horizontal and vertical motions were not independent processes but linked to the instantaneous deformation of the roller surface profile. The amplitudes of toe oscillations and depth fluctuations were enhanced with an increasing Froude number, while the dimensionless frequencies decreased [35]. For the same Froude number, the relationship between the maximum standard deviation of depth fluctuation along the roller $(y_s')_{max}$, and the standard deviation of jump toe oscillation x_t' can be estimated as $(y_s')_{max} = 1.36 \times x_t' - 0.82 \times d_1$. The ratio of corresponding frequencies was about $F_s/F_t \approx 2.5$. The effects of the Reynolds number were tested for $Fr_1 = 5.1$ and $2.1 \times 10^4 < Re < 1.6 \times 10^5$. The results are shown in Fig. 7a in terms of the amplitude and in Fig. 7b in terms of the frequency. The dimensionless amplitudes were independent of the Reynolds number, whereas the dimensionless frequencies increased with an increasing Reynolds number. That is, viscous scale effects were only observed in terms of the time scales of roller fluctuating motions. The dimensionless frequencies of unsteady fluctuations in prototype hydraulic jumps are expected to be higher than the values suggested by the existing experimental data.

4.2 Scale effects on air–water flow properties

Figure 8 illustrates the effects of Reynolds number on the void fraction and bubble count rate results. For each parameter, the vertical data profiles are presented for $Fr_1 = 3.8$ and 7.5, and the variations of the maximum value in the shear flow are shown. Chanson and

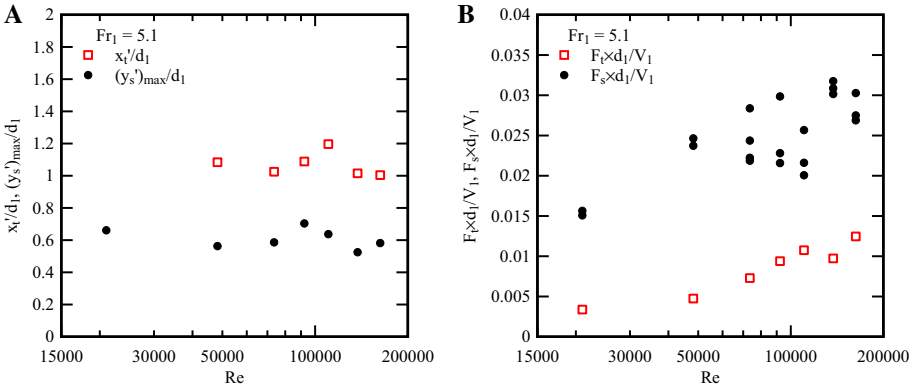

Fig. 7 Effect of Reynolds number on roller surface dynamics; $Fr_1 = 5.1$, $2.1 \times 10^4 < Re < 1.6 \times 10^5$. **a** *Left* dimensionless standard deviations of jump toe oscillation and water depth fluctuation as functions of Reynolds number. **b** *Right* characteristic jump toe oscillation and water depth fluctuation frequencies as functions of Reynolds number

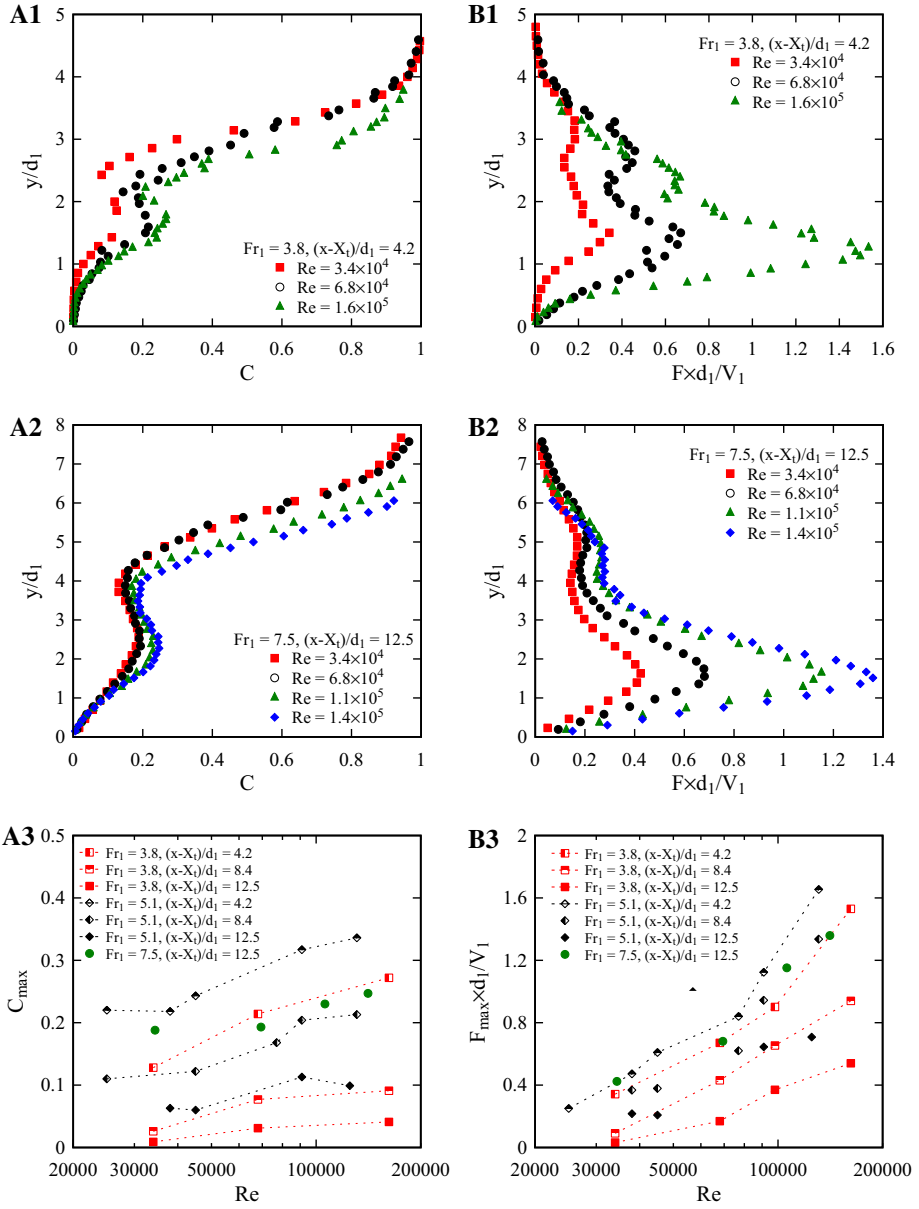

Fig. 8 Effects of Reynolds number on void fraction and bubble count rate. **a1** *Left* vertical void fraction distributions–$Fr_1 = 3.8$, $(x - X_t)/d_1 = 4.2$. **b1** *Right* vertical bubble count rate distributions–$Fr_1 = 3.8$, $(x - X_t)/d_1 = 4.2$. **a2** *Left* vertical void fraction distributions–$Fr_1 = 7.5$, $(x - X_t)/d_1 = 12.5$. **b2** *Right* vertical bubble count rate distributions–$Fr_1 = 7.5$, $(x - X_t)/d_1 = 12.5$. **a3** *Left* local maximum void fraction in turbulent shear layer as a function of Reynolds number, inclusive of data of Chanson and Gualtieri [11], Murzyn and Chanson [24], Chachereau and Chanson [8]. **b3** *Right* maximum bubble count rate in turbulent shear layer as a function of Reynolds number, inclusive of data of Chanson and Gualtieri [11], Murzyn and Chanson [24], Chachereau and Chanson [8]

Chachereau [10] presented a series of comparisons for $Fr_1 = 5.1$ based on the data of Chanson and Gualtieri [11], Murzyn and Chanson [24], Chachereau and Chanson [8]. Their flow conditions were also repeated in the present study. The results indicated some increase in shear layer void fraction with increasing Reynolds number. This might be linked to the change of inflow turbulence level which is critical for the air entrapment at the impingement point. For a rough estimate of void fraction distribution, the scale effects appeared to be not crucial for Reynolds numbers larger than 4×10^4 to 6×10^4. On the other hand, the significance of Reynolds number affecting the shear layer bubble count rate can be understood by considering the formation and breakage of air bubbles determined by the balance between air–water surface tension and viscous shear stress. The drastic scale effects in terms of bubble count rate implied much stronger air–water exchange and bubble-turbulence interaction in prototype flows than in laboratory models. For example, a hydraulic jump in prototype stilling basin with $Re \sim 10^7$ may produce one to two orders more bubbles compared to an experimental jump with $Re \sim 10^5$, though such an estimate still needs to be justified by prototype measurements.

The ratio of time-averaged void fraction to bubble count rate yields the mean bubble chord time which is the average time a bubble spends on the phase-detection probe tip. The bubble chord length can be derived in the lower shear flow where the velocity is constantly in the longitudinal downstream direction. In the upper part of the roller, the time-averaged longitudinal velocity data do not provide useful information on length scale of bubbles. The mean bubble chord time increased across a vertical cross-section from bottom to free-surface. It was sensitive to the change in Reynolds number. For example, at the elevation of maximum bubble count rate $y = Y_{Fmax}$, the present data suggested a relationship between the dimensionless mean bubble chord time and Reynolds number: $(t_{ch})_{mean} \times V_1/d_1 = 1.5 \times 10^4/Re$. The bubble chord length exhibited a broad spectrum in its probability distribution. Figure 9 presents the probability density functions (PDFs) of bubble chord length at the elevation $y = Y_{Fmax}$ for different Reynolds numbers. The bin size of PDF is 0.5 mm. The probability distribution indicated a wide range of bubble size from sub-millimetre to centimetre. For the tested flow conditions at such location of maximum shear stress, more than 50 % of bubbles had a chord length smaller than 2 mm. A higher

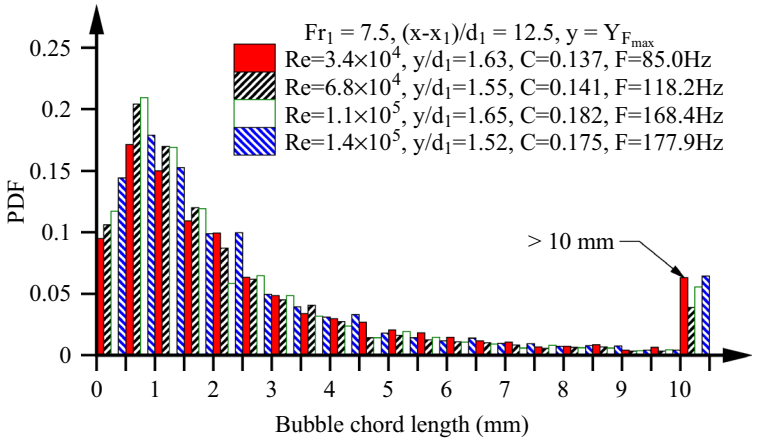

Fig. 9 Effect of Reynolds number on probability distribution of bubble chord length at the elevation of maximum bubble count rate–$Fr_1 = 7.5$, $(x - X_t)/d_1 = 12.5$, $y = Y_{Fmax}$

Reynolds number tended to produce a larger percentage of small-size bubbles due to the enhanced turbulent shear force that induced break-up of large bubbles.

4.3 Scale effects on turbulent scales

4.3.1 Turbulence intensity

No obvious scale effects were observed in terms of dimensionless time-averaged interfacial velocity. The derivation of turbulence intensity Tu was based upon an assumption of a random detection of an infinitely large number of air–water interfaces, although bubble grouping and large-scale fluctuations did exist and might bias the measurement results. The raw phase-detection probe signal often gave unusually-high turbulence intensity in the flow regions affected by the large-scale fluctuations. The high-pass filtered signal allowed for a more accurate and meaningful characterisation of decomposed turbulence intensity Tu″ between 0.5 and 1.8, decreasing in the streamwise direction. Such air–water interfacial turbulence intensities were larger than the water-phase turbulence intensities measured in less aerated jumps [21, 31]. Figure 10 compares the high-frequency turbulence intensities Tu" for different Reynolds numbers ($Fr_1 = 3.8$ and 7.5). A smaller turbulence intensity Tu″ was shown for lower Reynolds number, implying an underestimated turbulence level in a down-scaled model. For example, for $Fr_1 = 7.5$ at the elevation of maximum bubble count rate $y = Y_{Fmax}$, Tu″ decreased by 20 % when the Reynolds number was reduced from 1.4×10^5 to 3.4×10^4. The decrease in relative velocity fluctuation was linked to the increasing significance of viscous force when the Reynolds number was small, which was also responsible for a decrease in local shear stress.

4.3.2 Integral turbulent length scales

The integral turbulent length scale was measured in the longitudinal direction. A typical data profile showed a quasi-bimodal shape in a vertical cross-section close to the jump toe. The lower peak was exhibited around the elevation of maximum velocity in the lower shear

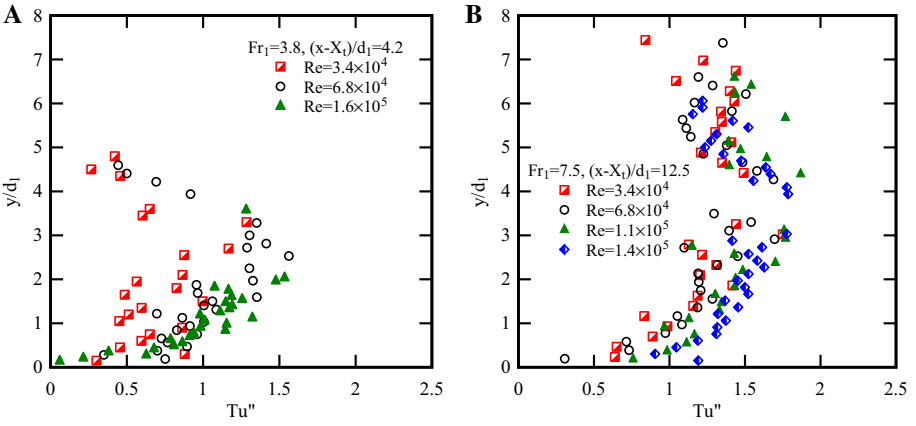

Fig. 10 Effect of Reynolds number on turbulence intensities of high-frequency filtered signals. **a** *Left* $Fr_1 = 3.8$, $(x - X_t)/d_1 = 4.2$. **b** *Right* $Fr_1 = 7.5$, $(x - X_t)/d_1 = 12.5$

flow, and the upper peak was seen next to the roller surface. The two peaks characterised respectively the large high-frequency turbulent structures in the shear flow and the low-frequency free-surface structures associated with the roller surface deformation. This can be seen in Fig. 11 showing both integral length scales L_X/d_1 and L_X''/d_1 for the raw and high-pass filtered signals. The close values of L_X/d_1 and L_X''/d_1 in the lower shear flow indicated dominant high-frequency turbulent motions in this region, whereas the large difference between L_X/d_1 and L_X''/d_1 next to the free-surface implied a main contribution of local low-frequency fluctuations. While the lower peak shrunk rapidly at downstream as the high-frequency turbulence was dissipated, the upper peak increased as the surface wave propagated and large roller structures formed along the roller free-surface. Murzyn et al. [27] calculated the integral turbulent length scales for instantaneous water surface position data Y_s. The surface integral length scales were close to the present bubbly-flow integral length scales measured at $y = Y_{50}$, noting that $Y_{50} \approx Y_s$ (Eq. (18)).

Figure 11 demonstrates the scale effects on longitudinal integral length scales for four Reynolds numbers. The variation of each dimensionless length scale was limited for $Re > 6.8 \times 10^4$, and a further decrease in Reynolds number led to a remarkable increase in length scales in the upper shear layer and free-surface region. This was because the large vortical and recirculating flow structures were dissipated rapidly for a small Reynolds number. The vortical and recirculating structures were responsible for a deterioration of signal correlation (e.g. R_{ij} in Eq. 1), thus led to smaller integral turbulent scales. In other words, the increase in integral turbulent scales at small Reynolds numbers was the result of a better-organised, less turbulent flow pattern.

4.4 Scale effects on two-dimensional bubble clustering

A result of bubble-turbulence interaction is the grouping of bubbles, forming bubble clusters. The bubble clustering events in hydraulic jumps were investigated previously based on various clustering criteria that identified one-dimensional bubble clusters in the longitudinal direction. For example, the near-wake criterion defines a pair of clustering bubbles travelling one after another when their separation distance was smaller than the dimension of the leading bubble. A two-dimensional near-wake criterion was developed to

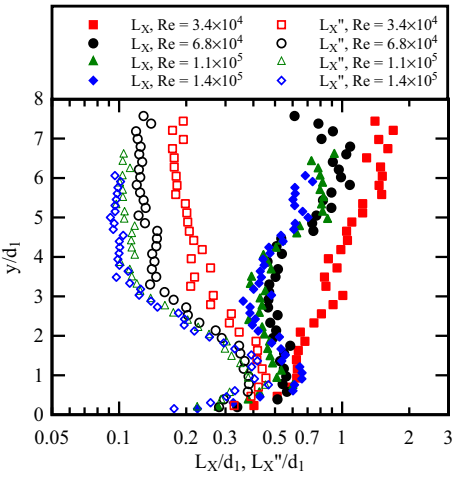

Fig. 11 Effect of Reynolds number on longitudinal integral turbulent length scale–$Fr_1 = 7.5$, $(x - X_t)/d_1 = 12.5$

take into account bubbles travelling side by side [35]. Figure 12 sketches a two-dimensional cluster structure detected by two phase-detection probe sensors separated by a transverse distance Δz. Herein the effects of Reynolds number were investigated for $Fr_1 = 7.5$ with a probe sensor separation $\Delta z = 3.57$ mm. The typical results are presented in Fig. 13a–d at the location $(x - X_t)/d_1 = 12.5$, $y = Y_{Fmax}$, with comparison of the two-dimensional cluster properties to the one-dimensional properties given by a single probe sensor.

Figure 13a shows the dimensionless cluster rate $F_{clu} \times d_1/V_1$ defined as the number of clusters per second. The cluster rate was found to be proportional to the bubble count rate hence also increase with increasing Reynolds number. Figures 13b, c show respectively the cluster size N_{clu} defined as the average number of bubbles per cluster, and the cluster proportion P_{clu} defined as the percentage of bubbles in clusters. The percentage of medium to large clusters that consisted of four or more bubbles is plotted in Fig. 13d. Scale effects were observed for all parameters based on both one-dimensional and two-dimensional clustering criteria. Basically, the results indicated that, for a larger Reynolds number, a larger proportion of bubbles were involved in clustering events, forming more clusters per unit time and each cluster consisting of more bubbles on average. A comparison in terms of the bubble chord time spectrum further indicated that an increase in Reynolds number led to a greater percentage of small bubble chord time for the family of bubbles involved in clustering. It implied that a higher turbulence level involved more small bubbles in clustering events, thus enhanced the bubble-turbulence interplay. Overall, the clustering properties showed strong correlation to the turbulence level of the flow, and were hardly reproduced in down-scaled models based upon Froude similitude. The findings was supported by the earlier preliminary findings of Chanson and Chachereau [10].

4.5 Summary: data extrapolation to full-scale and scale effects

The present study demonstrated that most air–water flow properties obtained with laboratory experiments cannot be directly extrapolated to full scale based upon Froude similarity. The results highlighted a wide range of characteristics related to flow dynamics, turbulence, air entrainment and bubble-turbulence interaction that should be considered in scale effect assessment. Table 2 summarises the tested flow properties.

When the scale effects are investigated using the same experimental flume, a challenge exists in characterising the inflow turbulence level which is critical to the air entrainment at the jump toe. Although the inflow length over which the boundary layer develops can be scaled accordingly, the turbulence level of the impinging flow may be also affected by the initial flow in upstream head tank, the inflow aspect ratio and the relative roughness of the channel bed. These factors are not scaled and their effects on the experimental results are often ignored. Furthermore, the effects of the instrumentation characteristics have not been

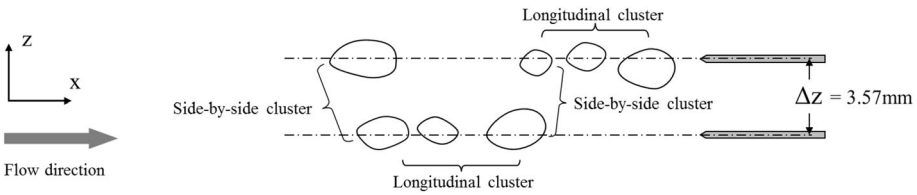

Fig. 12 Sketch of a two-dimensional bubble cluster detected by side-by-side phase-detection probe sensors

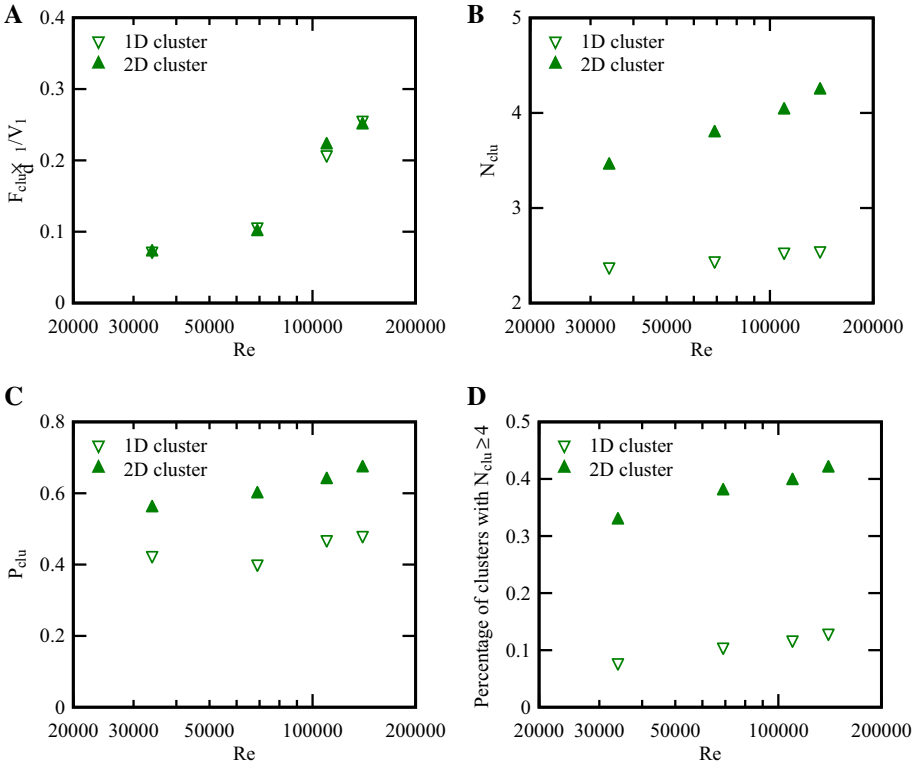

Fig. 13 Effect of Reynolds number on longitudinal and two-dimensional clustering characteristics– $Fr_1 = 7.5$, $(x - X_t)/d_1 = 12.5$, $y = Y_{Fmax}$. **a** *Left* cluster rate F_{clu} defined as the number of clusters per second. **b** *Right* average cluster size N_{clu} defined as the average number of bubbles per cluster. **c** *Left* cluster proportion P_{clu} defined as the percentage of bubbles in clusters. **d** *Right* percentage of clusters consisting of more than three bubbles

studied systematically up to date. The minimum size of detectable bubbles/droplets is linked to the relative size and scanning rate of the phase-detection probe sensor. The particles smaller than the sensor inner diameter in length scale or the response time in time scale are missed by the measurement system. When a double-tip phase-detection probe is in use, the relative position of two sensor tips is another factor to be taken into account.

5 Conclusion

The hydraulic jumps were studied physically in terms of free-surface dynamics, air–water flow properties and turbulent scales for Froude numbers between 3.8 and 10. The scale effects were investigated for three Froude numbers, with corresponding Reynolds numbers ranging from 2.1×10^4 to 1.6×10^5. Most flow properties were tested within the length of jump roller which was a function of the Froude number. Some flow properties showed self-similar evolution trend along the roller between different flow conditions. These included the water surface elevation, maximum shear layer void fraction, maximum interfacial velocity and their vertical positions. As a result, analytical expressions of void fraction and

Table 2 Criteria to minimise scale effects in physical scaling of hydraulic jumps based on Froude similarity

Flow properties	Dimensionless notation	Remarks
Height and length of jump roller	d_2/d_1, $L_r/d_1 = F(Fr_1)$	No scale effects
Roller surface elevation	$Y_s/d_1 = F((x - X_t)/d_1, Fr_1)$	Self-similarity. No scale effects
Amplitudes of toe oscillation and depth fluctuation	x_t'/d_1, $(y_s')_{max}/d_1 = F(Fr_1)$	No scale effects
Frequencies of toe oscillation and depth fluctuation	$F_t \times d_1/V_1$, $F_s \times d_1/V_1 = F(Fr_1, Re)$	Limited scale effects for $Re > 1 \times 10^5$
Void fraction	$C \approx F((x - X_t)/d_1, y/d_1, Fr_1)$	Quasi-self-similarity. Limited scale effects for $Re > 4 \times 10^4$ to 6×10^4 C_{max}, Y_{Cmax}/d_1, Y_{50}/d_1, $D^{\#}$, $D^* \approx F((x - X_t)/d_1, Fr_1)$
Bubble count rate	$F \times d_1/V_1 = F((x - X_t)/d_1, y/d_1, Fr_1, Re)$	Scale effects unless at full-scale
Bubble chord time	$t_{ch} \times V_1/d_1 = F((x - X_t)/d_1, y/d_1, Fr_1, Re)$	Scale effects unless at full-scale
Interfacial velocity	$V/V_1 = F((x - X_t)/d_1, y/d_1, Fr_1)$	Self-similarity with flow reversal. No scale effects V_{max}/V_1, Y_{Vmax}/d_1, $Y_{0.5}/d_1$, $V_{recirc}/V_1 = F((x - X_t)/d_1, Fr_1)$
High-frequency interfacial turbulence intensity	$Tu'' = F((x - X_t)/d_1, y/d_1, Fr_1, Re)$	Scale effects unless at full-scale
Integral turbulent length scale	L_X/d_1, $L_X''/d_1 = F((x - X_t)/d_1, y/d_1, Fr_1, Re)$	Limited scale effects for $Re > 4 \times 10^4$ to 6×10^4
Air entrainment flux	$q_{ent}/(Q/W) \approx F((x - X_t)/d_1, Fr_1)$	Limited scale effects for $Re > 4 \times 10^4$ to 6×10^4
Bubble clustering properties	$F_{clu} \times d_1/V_1$, N_{clu}, $P_{clu} = F((x - X_t)/d_1, y/d_1, Fr_1, Re)$	Scale effects unless at full-scale

interfacial velocity profiles could be defined by the longitudinal position $(x - X_t)/d_1$ and Froude number Fr_1, ignoring the limited scale effects on shear layer void fraction for small Reynolds numbers. For most other parameters, noticeable scale effects were observed and key results are presented in Table 2. While the characteristic surface fluctuation frequencies, shear layer void fraction and integral turbulent length scales were mainly affected at Reynolds numbers of order of 10^4 or less, the bubble count rate, bubble chord time, bubble clustering and turbulence intensities were drastically influenced by downscaling and could be only correctly quantified at full-scale. In practice, the aeration level and turbulent scales might be estimated with satisfactory accuracy for engineering applications given a Reynolds number no less than 4×10^4 to 6×10^4.

The present study broadened the list of scale-sensitive parameters in such turbulent two-phase open channel flows by encompassing the unsteady free-surface motions, turbulent length/time scales and two-dimensional bubble clustering events. No numerical model has been fully validated for these flow properties up to date. Although the prediction of some key steady flow properties is now possible for permissive accuracy requirement, most dynamic data and turbulence statistics are still not available for prototype conditions.

Besides the presented flow properties, one parameter of equivalent importance, if not more, is the pressure fluctuations, as well as the associated modification of unsteady pressure field by the air–water mixing.

Acknowledgments The authors thank Jason Van Der Gevel and Stewart Matthews, School of Civil Engineering, The University of Queensland for their technical assistance. The post-processing of phase-detection probe signal was facilitated by the software developed by Dr Stefan Felder (University of New South Wales). The research project was supported by the Australian Research Council (Grant DP120100481). The first author acknowledges the advisory input of Dr Frédéric Murzyn (ESTACA Laval, France) during his Ph.D. thesis.

References

1. Barenblatt GI (1996) Scaling, self-similarity, and intermediate asymptotics. Cambridge University Press, UK
2. Bélanger JB (1841) Notes sur l'hydraulique (Notes on hydraulic engineering). Ecole Royale des Ponts et Chaussées, Paris **(in French)**
3. Bidone G (1819) Le remou et sur la propagation des ondes (The jump and on the wave propagation). Rep R Acad Sci Turin 12:21–112 **(in French)**
4. Bin AK (1993) Gas entrainment by plunging liquid jets. Chem Eng Sci 48(21):3585–3630
5. Brattberg T, Chanson H (1998) Air entrainment and air bubble dispersion at two-dimensional plunging water jets. Chem Eng Sci 53(24):4113–4127
6. Brattberg T, Chanson H, Toombes L (1998) Experimental investigations of free-surface aeration in the developing flow of two-dimensional water jets. J Fluid Eng 120(4):738–744
7. Cain P, Wood IR (1981) Measurements of self-aerated flow on spillways. J Hydraul Division 107(HY11):1425–1444
8. Chachereau Y, Chanson H (2011) Bubbly flow measurements in hydraulic jumps with small inflow Froude numbers. Int J Multiph Flow 37(6):555–564. doi:10.1016/j.ijmultiphaseflow.2011.03.012
9. Chanson H (2010) Convective transport of air bubbles in strong hydraulic jumps. Int J Multiph Flow 36(10):798–814. doi:10.1016/j.ijmultiphaseflow.2010.05.006
10. Chanson H, Chachereau Y (2013) Scale effects affecting two-phase flow properties in hydraulic jump with small inflow Froude number. Exp Therm Fluid Sci 45:234–242. doi:10.1016/j.expthermflusci.2012.11.014
11. Chanson H, Gualtieri C (2008) Similitude and scale effects of air entrainment in hydraulic jumps. J Hydraul Res 46(1):35–44
12. Chanson H, Toombes L (2002) Air-water flows down stepped chutes: turbulence and flow structure observations. Int J Multiph Flow 28(11):1737–1761
13. Coakley DB, Haldeman PM, Morgan DG, Nicolas KR, Penndorf DR, Wetzel LB, Weller CS (2001) Electromagnetic scattering from large steady breaking waves. Exp Fluids 30:479–487
14. Hager WH (1992) Energy dissipators and hydraulic jump. Kluwer Academic Publishers, Dordrecht
15. Henderson FM (1966) Open channel flow. MacMillan Company, New York
16. Hoyt JW, Sellin RHJ (1989) Hydraulic jump as 'mixing layer'. J Hydraul Eng 40(3):1607–1614
17. Kucukali S, Chanson H (2008) Turbulence measurements in hydraulic jumps with partially-developed inflow conditions. Exp Therm Fluid Sci 33(1):41–53. doi:10.1016/j.expthermflusci.2008.06.012
18. Liggett JA (1994) Fluid mechanics. McGraw-Hill, New York
19. Lighthill J (1978) Waves in fluid. Cambridge University Press, Cambridge
20. Lin C, Hsieh S, Lin I, Chang K, Raikar R (2012) Flow property and self-similarity in steady hydraulic jumps. Exp Fluids 53:1591–1616. doi:10.1007/s00348-012-1377-2
21. Liu M, Rajaratnam N, Zhu D (2004) Turbulent structure of hydraulic jumps of low Froude numbers. J Hydraul Eng 130(6):511–520
22. Long D, Rajaratnam N, Steffler PM, Smy PR (1991) Structure of flow in hydraulic jumps. J Hydraul Res 29(2):207–218
23. Montes SJ (1998) Hydraulics of open channel flow. ASCE Press, New York
24. Murzyn F, Chanson H (2008) Experimental assessment of scale effects affecting two-phase flow properties in hydraulic jumps. Exp Fluids 45(3):513–521. doi:10.1007/s00348-008-0494-4
25. Murzyn F, Chanson H (2009) Experimental investigation of bubbly flow and turbulence in hydraulic jumps. Environ Fluid Mech 9(2):143–159. doi:10.1007/s10652-008-9077-4

26. Murzyn F, Mouaze D, Chaplin JR (2005) Optical fibre probe measurements of bubbly flow in hydraulic jumps. Int J Multiph Flow 31(1):141–154. doi:10.1016/j.ijmultiphaseflow.2004.09.004
27. Murzyn F, Mouaze D, Chaplin JR (2007) Air-water interface dynamic and free surface features in hydraulic jumps. J Hydraul Res 45(5):679–685. doi:10.1080/00221686.2007.9521804
28. Prosperetti A, Tryggvason G (2009) Computational methods for multiphase flow. Cambridge University Press, London
29. Rajaratnam N (1962) An experimental study of air entrainment characteristics of the hydraulic jump. J Instr Eng India 42(7):247–273
30. Rajaratnam N (1965) The hydraulic jump as a wall jet. J Hydraul Div 91(HY5):107–132
31. Resch FJ, Leutheusser HJ (1972) Le ressaut hydraulique: mesures de turbulence dans la région diphasique (The hydraulic jump: turbulence measurements in the two-phase flow region). La Houille Blanche 4:279–293 **(in French)**
32. Richard GL, Gavrilyuk SL (2013) The classical hydraulic jump in a model of shear shallow-water flows. J Fluid Mech 725:492–521. doi:10.1017/jfm.2013.174
33. Subramanya K (2009) Flow in open channels. Tata McGraw-Hill Education, New Delhi
34. Svendsen IA, Veeramony J, Bakunin J, Kirby JT (2000) The flow in weak turbulent hydraulic jumps. J Fluid Mech 418:25–57
35. Wang H (2014) Turbulence and air entrainment in hydraulic jumps. PhD thesis. School of Civil Engineering, The University of Queensland, Brisbane. doi: 10.14264/uql.2014.542
36. Wang H, Felder S, Chanson H (2014) An experimental study of turbulent two-phase flow in hydraulic jumps and application of a triple decomposition technique. Exp Fluids 55(7):1775. doi:10.1007/s00348-014-1775-8
37. Wood IR (1991) Air entrainment in free-surface flows. IAHR Hydraulic Structures Design Manual No. 4, Hydraulic Design Considerations. Balkema Publisher, Rotterdam